crystals

MDPI

Article

Electrolyte-Dependent Electrochemical Exfoliation of MoS_2 Nanosheets and Its Impact on Nonlinear Optical Limiting

Xuefeng Chu [1,2], Siming Qiao [1,2], Haiyang Zhao [3,*], Bingxue Li [4], Junjie Pan [4], Longyu Guo [5], Dingxuan Zhang [4], Chao Wang [1,2], Sa Lv [1,2], Faxin Peng [1,2], Haoran Niu [1,2], Xuan Fang [4,*] and Xiaotian Yang [3]

1 Key Laboratory of Architectural Cold Climate Energy Management, Ministry of Education, Jilin Jianzhu University, Changchun 130118, China; stone2009@126.com (X.C.); 13153807860@163.com (S.Q.); wangchao@jlju.com (C.W.); lvsa@jlju.edu.cn (S.L.); 18574368242@163.com (F.P.); 19990552997@163.com (H.N.)
2 School of Electrical and Computer Science, Jilin Jianzhu University, Changchun 130118, China
3 Department of Chemistry, Jilin Normal University, Siping 136000, China; hanyxt@163.com
4 School of Physics, Changchun University of Science and Technology, Changchun 130022, China; 2024200042@mails.cust.edu.cn (B.L.); pjj18943122097@163.com (J.P.); zdxqwer134@163.com (D.Z.)
5 Electron Microscopy Center, Jilin University, Changchun 130012, China; guolongyu@jlu.edu.cn
* Correspondence: zhaohaiyang4809@163.com (H.Z.); fangx@cust.edu.cn (X.F.)

Abstract

Electrochemical exfoliation is an efficient approach for producing MoS_2 nanosheets, yet the correlation between exfoliation conditions, structural evolution, and nonlinear optical (NLO) properties remains insufficiently understood. In this work, MoS_2 nanosheets were prepared using two representative electrolyte systems, acetonitrile/TPABr and aqueous Na_2SO_4, under controlled voltages. The results reveal distinct exfoliation mechanisms, where ion intercalation dominates in the nonaqueous system, while bubble-assisted processes prevail in the aqueous system. Structural and chemical analyses (Raman, XRD, EDS, and XPS) demonstrate that the nonaqueous system yields MoS_2 with higher crystallinity and lower oxidation degree, whereas the aqueous system shows increased oxidation with the coexistence of Mo^{5+} and Mo^{6+} species. Correspondingly, enhanced nonlinear absorption and optical limiting performance are observed. A clear mechanism–structure–property relationship is established, highlighting the critical role of electrolyte environment and applied voltage in tailoring NLO responses. This work provides insights into the controlled preparation of MoS_2 nanosheets for photonic and optoelectronic applications.

Keywords: MoS_2 nanosheets; electrochemical exfoliation; electrolyte-dependent; reverse saturable absorption; optical limiting; Z-scan

Check for updates

Academic Editor: Vladislav V. Kharton

Received: 26 March 2026
Revised: 25 April 2026
Accepted: 30 April 2026
Published: 2 May 2026

Copyright: © 2026 by the authors. Licensee MDPI, Basel, Switzerland. This article is an open access article distributed under the terms and conditions of the Creative Commons Attribution (CC BY) license.

1. Introduction

Two-dimensional transition metal dichalcogenides (2D TMDCs), featuring layered van der Waals structures and strong excitonic effects, have attracted extensive attention for applications in electronics, sensing, and optoelectronics. Among them, molybdenum disulfide (MoS_2) is one of the most representative semiconducting TMDCs. When thinned from bulk to monolayer or few-layer structures, MoS_2 undergoes a transition from an indirect to a direct band gap, resulting in enhanced photoluminescence and tunable optical absorption [1–3]. Under intense optical excitation, MoS_2 also exhibits pronounced third-order nonlinear optical responses, including saturable absorption (SA), reverse saturable absorption (RSA), and optical limiting (OL), making it highly promising for laser protection, optical switching, and nonlinear photonic devices. The performance of MoS_2 in such

applications strongly depends on the availability of high-quality, scalable monolayer or few-layer nanosheets. Various preparation methods have been developed, including mechanical exfoliation, chemical vapor deposition, liquid-phase ultrasonic exfoliation, chemical intercalation, and electrochemical exfoliation (ECE) [4–7]. Among these, ECE has emerged as an effective top-down strategy due to its rapid processing, tunable conditions, relatively high yield, and scalability [8]. More importantly, compared with strongly reactive chemical intercalation methods, ECE enables better control over intercalation, exfoliation, and defect generation through the applied potential, electrolyte composition, and electrode configuration, thereby providing a practical route for tailoring the structure–property relationship of MoS_2 nanosheets.

The exfoliation behavior of MoS_2 during ECE is highly dependent on both the electrolyte environment and the polarity of the applied potential, which determine the dominant interfacial processes and consequently influence the layer number, lateral size, phase composition, and defect or doping level of the resulting products. In neutral aqueous electrolytes such as Na_2SO_4, the electrochemical process is often accompanied by gas evolution at the interface, generating species such as O_2, SO_2, or H_2 depending on the reaction conditions. The formation and growth of gas bubbles within the interlayer galleries produce a wedging effect that promotes interlayer expansion and cleavage, resulting in exfoliation. This mechanism is commonly referred to as bubble-assisted or gas-expansion-driven exfoliation [9,10]. However, relatively high applied potentials may also induce edge etching, oxidation, and defect formation, which can significantly alter optical absorption and carrier dynamics.

In contrast, in nonaqueous electrolytes such as acetonitrile containing tetraalkylammonium salts (e.g., tetrapropylammonium bromide, TPA^+Br^-), cathodic exfoliation typically proceeds via an ion-intercalation-driven mechanism. Under negative polarization, solvated TPA^+ cations intercalate into the MoS_2 interlayers, weaken the van der Waals interactions, and expand the interlayer spacing. Subsequent dispersion and mild mechanical treatment then yield few-layer or thinner nanosheets [11–14]. Compared with aqueous systems, nonaqueous media can suppress water-splitting side reactions and mitigate strongly oxidative environments. Moreover, the size and solvation structure of intercalating ions can be tuned, offering advantages in dispersibility, process control, and impurity management. These characteristics make nonaqueous systems particularly suitable for investigating how intercalants and potential windows affect nanosheet quality and optical properties.

The nonlinear optical properties of two-dimensional materials are commonly evaluated using the Z-scan technique due to its simple configuration and quantitative capability for analyzing third-order nonlinear absorption. In particular, open-aperture Z-scan is effective for probing nonlinear absorption processes and assessing optical limiting behavior. Under the excitation conditions employed in this work (532 nm, 6 ns pulse width, and 4.5 kHz repetition rate), MoS_2 nanosheets operate in the nanosecond high-fluence regime. In this regime, the reduction in transmittance, namely RSA behavior, is generally attributed to excited-state absorption (ESA), sequential two-photon absorption (TPA), and possibly free-carrier absorption and/or thermal accumulation effects, all of which enhance optical absorption and contribute to optical limiting [15–17]. Notably, the RSA strength and optical limiting threshold are highly sensitive to microstructural characteristics. The layer number and lateral size affect the absorption cross-section and excited-state dynamics; defects, edge states, and surface charge influence energy-level distribution and carrier trapping/relaxation pathways; and the phase composition (2H/1T/1T′) may further modify the nonlinear absorption coefficient and optical limiting response [18–20]. Therefore, establishing the relationship between exfoliation mechanism, microstructure, and nonlinear optical performance is of critical importance.

In this work, layered MoS_2 was electrochemically exfoliated in two representative electrolyte systems: nonaqueous MeCN/TPABr and aqueous Na_2SO_4. Cathodic potentials of −6.5 and −4.5 V were applied in the MeCN/TPABr system [21], while alternating bipolar potentials of ±6.5 and ±4.5 V were used in the aqueous Na_2SO_4 system. These conditions enable a comparative investigation of two distinct exfoliation pathways, namely ion-intercalation-driven exfoliation and bubble-assisted exfoliation. The structural and chemical evolution of the exfoliated nanosheets was examined using SEM, Raman, XRD, EDS, and XPS, and the nonlinear optical response was evaluated by open-aperture Z-scan and optical limiting measurements. By correlating exfoliation conditions with crystallinity, oxidation state, and nonlinear optical behavior, this study aims to establish a mechanism–structure–property relationship for electrochemically exfoliated MoS_2 nanosheets.

2. Experiment

2.1. Preparation of MoS_2 Nanosheets

Electrochemical exfoliation of layered MoS_2 was carried out in a three-electrode sys tem. Bulk MoS_2 (99.99%) (Zhongcheng New Materials Technology Co., Ltd., Tianjin, China) was cut into pieces of approximately 0.5 cm × 0.5 cm and used as the working electrode. A Pt foil and an Ag/AgCl electrode (Hangzhou Frank Technology Co., Ltd., Hangzhou, China) were employed as the counter and reference electrodes, respectively. To minimize contamination from the electrical contact, the MoS_2 electrode was connected using a copper strip, while the nonactive contact region was insulated, leaving only the MoS_2 surface exposed to the electrolyte.

Two electrolyte systems were used to investigate the effect of exfoliation mecha-nisms. In the nonaqueous system, acetonitrile containing tetrapropylammonium bromide (MeCN/TPABr) was employed, and cathodic potentials of −6.5 V and −4.5 V were applied under constant current–time (i–t) mode. In the aqueous system, Na_2SO_4 solution was used as the electrolyte, and exfoliation was performed under bipolar potentials of ±6.5 V and ±4.5 V (For the aqueous Na_2SO_4 electrolyte, bipolar chronoamperometric exfoliation was performed at ±6.5 V and ±4.5 V, with each anodic/cathodic step maintained for 5 s before reversing the polarity) using chronoamperometry (CA). The electrolytes used in this work were a 1.0 $mol \cdot L^{-1}$ aqueous Na_2SO_4 solution and a 3.0 $mmol \cdot L^{-1}$ TPABr/MeCN solution, which was prepared by dissolving 0.08 g of tetrapropylammonium bromide (TPABr) in 10 mL of acetonitrile. In all cases, the exfoliation duration was fixed at 1 h.

The applied potentials of 6.5 V and 4.5 V were selected based on both the instrumental limitations and the exfoliation characteristics of the aqueous Na_2SO_4 system. To ensure equal voltage amplitudes under bipolar operation, the maximum potential difference per-mitted by the electrochemical workstation (CHI760E, Shanghai Chenhua Instrument Co., Ltd., Shanghai, China) was 13 V, which set the upper limit at ±6.5 V. In addition, lower ap-plied voltages were found to be unfavorable for bubble-assisted exfoliation in Na_2SO_4 elec-trolyte, resulting in reduced exfoliation efficiency and increased oxidation of the nanosheets. Preliminary experiments further showed that when the applied voltage was below 4.5 V, corrosion of the working electrode occurred during exfoliation, introducing impurities into the solution and thereby lowering the purity of the obtained nanosheets. Therefore, 6.5 V and 4.5 V were chosen as the representative operating potentials in this work.

After exfoliation, the resulting black dispersions were collected and purified by re-peated centrifugation at 5000 rpm for 5 min per cycle (eight cycles in total) to remove residual electrolyte and impurities. The collected precipitates were then subjected to ul-trasonication (80 W) for 20 min to further disperse the nanosheets. Finally, the products were dried and stored under ambient conditions. The obtained samples were denoted by MoS_2–MeCN6.5, MoS_2–MeCN4.5, MoS_2–$Na_2SO_4$6.5, and MoS_2–$Na_2SO_4$4.5, respectively.

2.2. Structural and Chemical Characterization

The surface morphology and cross-sectional features of the nanosheets were examined using a JSM-7900F scanning electron microscope (SEM, EDS, JEOL Ltd., Tokyo, Japan). The crystal structure and crystallinity of the nanosheets were analyzed using a Rigaku Ultima IV multifunctional X-ray diffractometer (XRD, Rigaku Corporation, Tokyo, Japan). The chemical composition, valence states, and bonding configurations were analyzed using an ESCALAB 250 Xi X-ray photoelectron spectrometer (XPS, Thermo Fisher Scientific, MA, USA).

2.3. Preparation of MoS_2/PMMA Composite Samples

To evaluate the nonlinear optical properties, MoS_2 nanosheets were embedded into a poly(methyl methacrylate) (PMMA) matrix to form organic glass samples. Methyl methacrylate (MMA) was used as the monomer and 2,2′-azobisisobutyronitrile (AIBN) as the polymerization initiator. Specifically, 0.02 g of MoS_2 nanosheets, 10.35 g of MMA, and 0.04 g of AIBN were mixed and dispersed by ultrasonication for 20 min, followed by magnetic stirring for 2 h to ensure uniform dispersion. The mixture was then heated at 75 °C under stirring until increased viscosity was observed, and subsequently cast into a mold. Polymerization was carried out at 45 °C for 12 h. After cooling to room temperature, transparent MoS_2/PMMA organic glass samples with a thickness of ~1 mm were obtained.

2.4. Nonlinear Optical Measurements

The nonlinear optical properties of the MoS_2/PMMA samples were investigated using the open-aperture Z-scan technique. A Nd:YAG laser operating at 532 nm with a pulse width of 6 ns and a repetition rate of 4.5 kHz was used as the excitation source. The laser beam was divided into a reference beam and a measurement beam using a beam splitter. The measurement beam was focused by a convex lens and transmitted through the sample mounted on a motorized translation stage along the optical axis. The transmitted energy was recorded as a function of sample position [22].

To improve measurement reliability, each Z-scan measurement was performed twice (forward and reverse scans), and the results were averaged. The nonlinear absorption coefficient was extracted by fitting the experimental data. The nonlinear absorption coefficient β is used to describe the intensity-dependent absorption capability of a material under strong optical excitation. In this work, the positive β values indicate reverse saturable absorption behavior, and a larger β corresponds to a stronger intrinsic nonlinear absorption response [23].

3. Results and Discussion

3.1. Electrolyte-Dependent Exfoliation Behavior and Morphology Evolution

The morphology of the electrochemically exfoliated MoS_2 nanosheets was examined by SEM to evaluate the influence of electrolyte system and applied voltage. As shown in Figure 1, all samples display sheet-like morphologies, confirming the successful exfoliation of bulk MoS_2.

Nevertheless, noticeable morphological differences are observed among the samples. The MeCN/TPABr-derived samples contain more separated and fragmented nanosheet structures, particularly at −6.5 V, suggesting more effective interlayer separation. In contrast, the aqueous-Na_2SO_4-derived samples show more stacked aggregates, especially at ±4.5 V, indicating relatively limited exfoliation under lower-voltage conditions.

These observations are consistent with different exfoliation pathways. In the nonaqueous MeCN/TPABr system, exfoliation is mainly associated with ion intercalation, where solvated organic cations weaken interlayer van der Waals interactions. In the aqueous

Na_2SO_4 system, exfoliation is mainly related to gas-evolution-assisted layer expansion. The applied voltage further regulates the exfoliation efficiency by affecting ion insertion or bubble generation. Therefore, the morphological differences suggest that both electrolyte environment and applied voltage influence the exfoliation behavior.

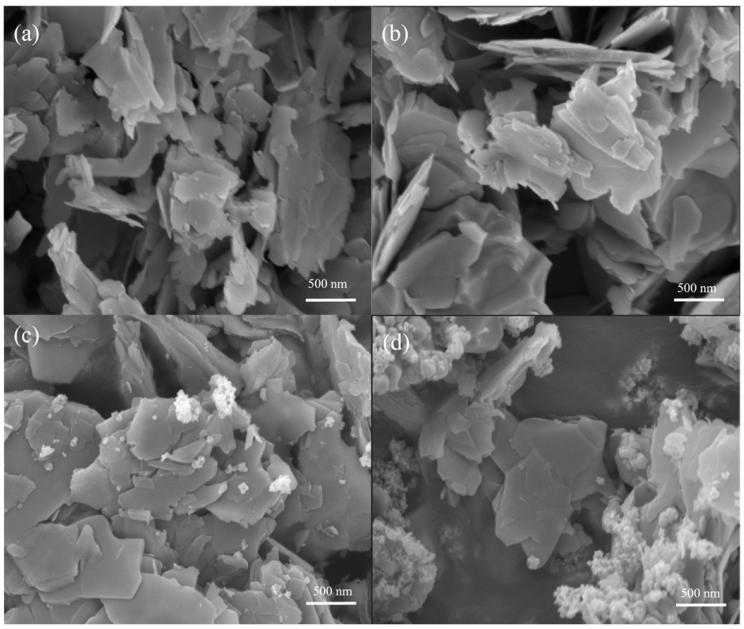


Figure 1. SEM images of electrochemically exfoliated MoS_2 nanosheets under different electrolyte systems and applied potentials: (**a**) MeCN −6.5 V, (**b**) MeCN −4.5 V, (**c**) Na_2SO_4 ±6.5 V, and (**d**) Na_2SO_4 ± 4.5 V.

3.2. Structural Integrity and Chemical State Evolution

The structural integrity and chemical states of the electrochemically exfoliated MoS_2 nanosheets were systematically investigated using Raman, XRD, EDS, and XPS, in order to elucidate the electrolyte-dependent evolution of crystallinity and oxidation.

Raman spectroscopy was used to evaluate lattice preservation and structural disorder after electrochemical exfoliation. As shown in Figure 2, all samples exhibit characteristic MoS_2 Raman modes located at approximately 380 and 403–405 cm^{-1}, corresponding to the E_2g^1 and A_1g modes, respectively. This indicates that the basic 2H-MoS_2 lattice framework is largely retained after exfoliation.

The MeCN/TPABr-derived samples show relatively stronger and sharper Raman peaks, suggesting better structural preservation. By contrast, the aqueous-Na_2SO_4-derived samples, especially the ±4.5 V sample, show weaker Raman features, implying increased structural disorder or reduced effective MoS_2 phase content. These results suggest that the nonaqueous electrolyte is more favorable for maintaining the MoS_2 lattice during exfoliation. The Raman results mainly serve to evaluate lattice preservation and structural disorder in this work.

The crystal structure of the exfoliated samples was further examined by XRD. As shown in Figure 3, all samples show a characteristic diffraction peak at $2\theta \approx 14.1°$, corresponding to the (002) plane of hexagonal 2H-MoS_2. Weak reflections at approximately 32.7°, 39.5°, 49.8°, and 58.3° can be indexed to the (100), (103), (105), and (110) planes, respectively, confirming the retention of the 2H-MoS_2 structure.

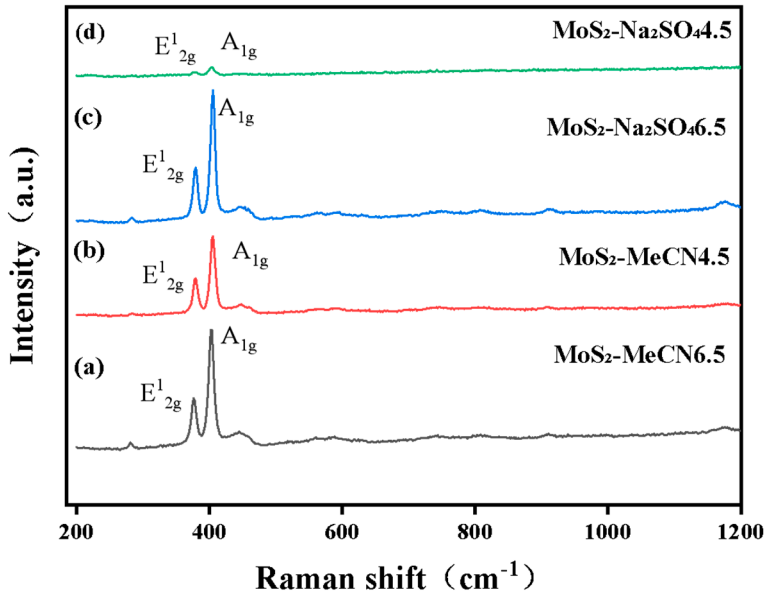


Figure 2. Raman patterns of (**a**) MoS_2–MeCN6.5, (**b**) MoS_2–MeCN4.5, (**c**) MoS_2–$Na_2SO_4$6.5, and (**d**) MoS_2–$Na_2SO_4$4.5.

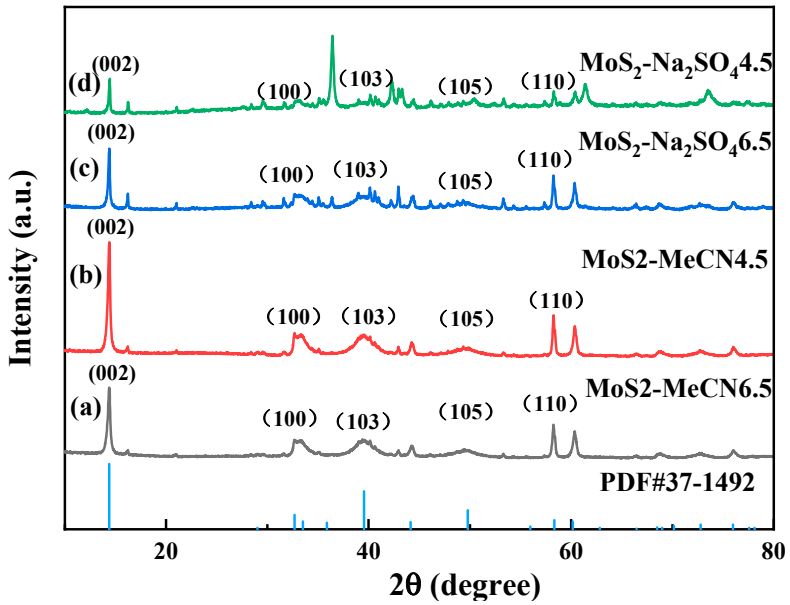


Figure 3. XRD patterns of (**a**) MoS_2–MeCN6.5, (**b**) MoS_2–MeCN4.5, (**c**) MoS_2–$Na_2SO_4$6.5, and (**d**) MoS_2–$Na_2SO_4$4.5.

Compared with the aqueous-Na_2SO_4-derived samples, the MeCN/TPABr-derived samples exhibit sharper and more intense diffraction peaks, indicating better crystallinity and stacking order. The broader and weaker peaks observed for the aqueous samples, especially at ±4.5 V, suggest increased disorder and reduced stacking coherence.

EDS analysis (Figure 4) further supports the above trend. EDS mapping confirms the presence and relatively uniform distribution of Mo and S in all samples. However, the oxygen signal differs significantly between the two electrolyte systems. The aqueous-Na_2SO_4-derived samples exhibit stronger oxygen signals than the MeCN/TPABr-derived samples, indicating a higher degree of oxidation in the aqueous environment. This is consistent with the involvement of water-related electrochemical side reactions during exfoliation.

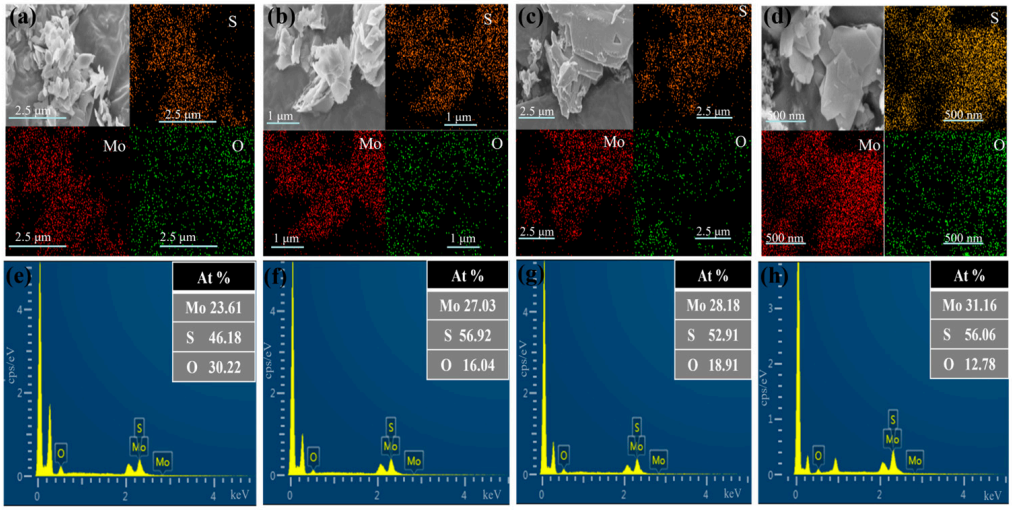


Figure 4. SEM images and EDS elemental mapping of MoS_2 nanosheets: (**a**) MoS_2–MeCN6.5, (**b**) MoS_2–MeCN4.5, (**c**) MoS_2–$Na_2SO_4$6.5, and (**d**) MoS_2–$Na_2SO_4$4.5 and EDS spectra and atomic percentages of S, Mo, and O: (**e**) MoS_2–MeCN6.5, (**f**) MoS_2–MeCN4.5, (**g**) MoS_2–$Na_2SO_4$6.5, and (**h**) MoS_2–$Na_2SO_4$4.5.

XPS was further employed to analyze the chemical states and quantify the oxidation evolution of the exfoliated MoS_2 nanosheets (Figures 5 and 6). The Mo 3d spectra of all samples can be deconvoluted into multiple components corresponding to Mo^{4+}, Mo^{5+}, and Mo^{6+} species, indicating the coexistence of different oxidation states after electrochemical exfoliation.

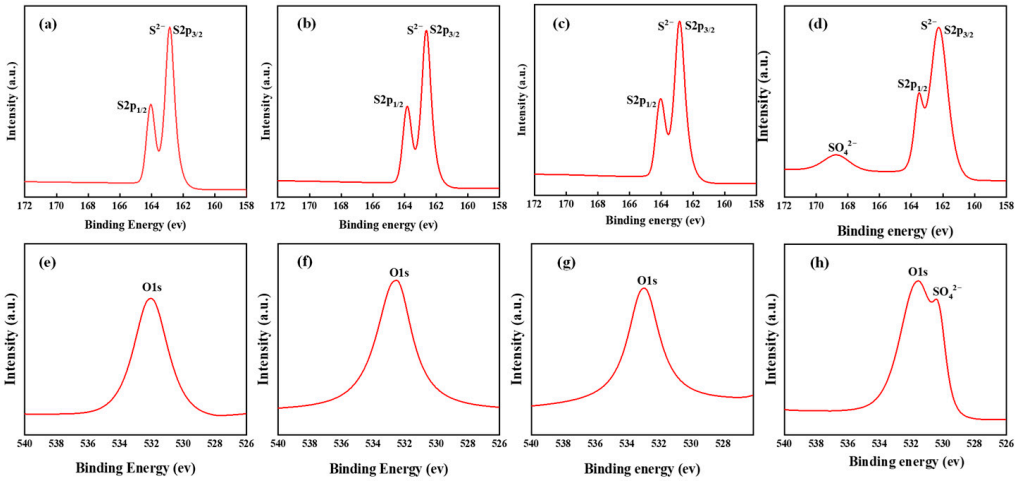


Figure 5. S2p of (**a**) MoS_2–MeCN6.5, (**b**) MoS_2–MeCN4.5, (**c**) MoS_2–$Na_2SO_4$6.5, and (**d**) MoS_2–$Na_2SO_4$4.5 and O1s of (**e**) MoS_2–MeCN6.5, (**f**) MoS_2–MeCN4.5, (**g**) MoS_2–$Na_2SO_4$6.5, and (**h**) MoS_2–$Na_2SO_4$4.5.

For the MeCN/TPABr-derived samples, the Mo 3d spectra are dominated by the Mo^{4+} doublet, with relatively small contributions from Mo^{5+} and Mo^{6+} components. Quantitative fitting results show that the combined fraction of oxidized species (Mo^{5+} + Mo^{6+}) remains low, indicating that most Mo atoms are preserved in the sulfide state. The S 2p spectra exhibit well-defined S^{2-} doublets without significant high-binding-energy features, and the O 1s signal is relatively weak, suggesting limited surface oxidation and good preservation of the Mo–S framework.

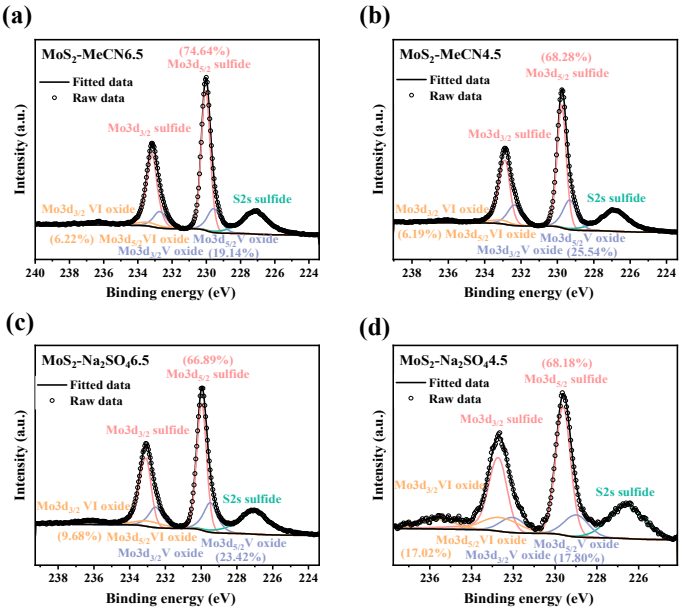


Figure 6. Mo 3d of (**a**) MoS_2–MeCN6.5, (**b**) MoS_2–MeCN4.5, (**c**) MoS_2–$Na_2SO_4$6.5, and (**d**) MoS_2–$Na_2SO_4$4.5.

In contrast, the aqueous-Na_2SO_4-derived samples exhibit a more complex chemical-state distribution. The Mo 3d spectra show a clear increase in both Mo^{5+} and Mo^{6+} components, and quantitative analysis reveals a significantly higher fraction of oxidized species compared with the MeCN/TPABr-derived samples. The presence of Mo^{5+} suggests the formation of intermediate oxidation states during electrochemical reactions, while the increased Mo^{6+} contribution indicates further oxidation toward oxide-like species. In addition, the S 2p spectra display additional high-binding-energy components associated with oxidized sulfur species, and the O 1s spectra show enhanced intensity, confirming the formation of oxygen-containing compounds. These features are particularly pronounced in the ±4.5 V sample, suggesting that insufficient exfoliation and prolonged interfacial reactions may promote oxidation under the present conditions.

The quantitative increase in Mo^{5+} and Mo^{6+} fractions indicates a progressive oxidation process from $Mo^{4+} \rightarrow Mo^{5+} \rightarrow Mo^{6+}$, reflecting the evolution of chemical states during electrochemical exfoliation. Such oxidation-induced modifications can introduce defect states, alter the local electronic structure, and reduce the effective MoS_2 active phase.

Combined with the Raman and XRD results, these observations suggest that the nonaqueous MeCN/TPABr system more effectively suppresses oxidation and preserves the intrinsic MoS_2 lattice, whereas the aqueous Na_2SO_4 system promotes partial oxidation and structural disorder. This difference in chemical-state evolution correlates well with the nonlinear optical measurements, where samples with lower fractions of oxidized species exhibit stronger nonlinear absorption and improved optical limiting performance.

3.3. Nonlinear Optical Properties and RSA Behavior

The nonlinear optical properties of the MoS_2/PMMA composites were investigated using the open-aperture Z-scan technique, based on an experimental configuration similar to that reported in our previous work [24]. A Nd:YAG laser operating at 532 nm with a pulse width of 6 ns and a repetition rate of 4.5 kHz was used as the excitation source. The laser beam was focused by a convex lens with a focal length of 10 cm, and the focused spot diameter at the sample position was approximately 90 μm, corresponding to a beam waist radius of $w_0 \approx 45\mu m$. The linear transmittance values of the PMMA plates containing MoS_2–MeCN6.5, MoS_2–MeCN4.5, MoS_2–$Na_2SO_4$6.5, and MoS_2–$Na_2SO_4$4.5 were measured

to be 0.430, 0.623, 0.603, and 0.641, respectively. The fitting was performed under the standard Gaussian-beam approximation.

The laser beam was divided into a reference beam and a measurement beam, and the corresponding signals were recorded by Detector 1 (D1) and Detector 2 (D2), respectively. To exclude the contribution of the PMMA matrix, a blank PMMA plate with the same thickness as the composite samples was used as the normalization reference. The experimentally measured normalized transmittance was defined as

$$T_{\mathrm{exp}}(z) = \frac{P_2(z)/P_1(z)}{P_{2,0}/P_{1,0}} \tag{1}$$

where $P_1(z)$ and $P_2(z)$ are the powers recorded by D1 and D2 at sample position z, respectively, and $P_{1,0}$ and $P_{2,0}$ are the corresponding powers measured using a blank PMMA plate of the same thickness under identical experimental conditions.

If the average incident power on the sample is denoted by P, the single-pulse energy is $E_p = P/f$, and the corresponding on-axis peak intensity at focus is given by

$$I_0 = \frac{E_p}{\pi w_0^2 \tau} \tag{2}$$

where f is the repetition rate and τ is the pulse duration. Under the Gaussian-beam approximation, the Rayleigh length is

$$z_0 = \frac{\pi w_0^2}{\lambda} \tag{3}$$

where λ is the laser wavelength. Using $w_0 \approx 45\mu$m and $\lambda = 532$ nm, the Rayleigh length was estimated to be $z_0 \approx 12$ mm, which is much larger than the sample thickness ($L = 1$ mm). Therefore, the thin-sample condition required for standard open-aperture Z-scan analysis is satisfied.

The linear absorption coefficient and effective thickness are given by

$$\alpha_0 = -\frac{\ln T_a}{L} \tag{4}$$

and

$$L_{\mathrm{eff}} = \frac{1 - \exp(-\alpha_0 L)}{\alpha_0} \tag{5}$$

where T_a is the linear transmittance and L is the geometric thickness of the sample.

Since all measured open-aperture Z-scan curves exhibited typical reverse saturable absorption (RSA) behavior, and no saturation term was included in the MATLAB R2023b fitting procedure, the experimental data were analyzed using an RSA-only model. In this case, the intensity-dependent absorption coefficient can be written as

$$\alpha(I) = \alpha_0 + \beta I \tag{6}$$

where β is the nonlinear absorption coefficient.

The on-axis intensity distribution along the propagation direction is

$$I(z) = \frac{I_0}{1 + (z/z_0)^2} \tag{7}$$

and the corresponding nonlinear absorption parameter is

$$q_0(z) = \beta I(z) L_{\text{eff}} = \frac{\beta I_0 L_{\text{eff}}}{1 + (z/z_0)^2} \tag{8}$$

Under the standard open-aperture Z-scan formalism, the theoretical normalized transmittance is expressed as

$$T_{\text{fit}}(z) = \frac{1}{\sqrt{\pi}\, q_0(z)} \int_{-\infty}^{+\infty} \ln\left[1 + q_0(z) e^{-\xi^2}\right] d\xi \tag{9}$$

where ξ is a dimensionless integration variable. In the MATLAB fitting procedure, the normalized coordinate $Z = z/z_0$ was used, and the theoretical transmittance $T_{\text{fit}}(z)$ was fitted to the experimental normalized transmittance $T_{\text{exp}}(z)$. Finally, the nonlinear absorption coefficient β was obtained from the fitting results. A positive β value indicates RSA behavior, and a larger β corresponds to a stronger intrinsic nonlinear absorption response.

As shown in Figure 7, all MoS_2/PMMA composites exhibit a decrease in normalized transmittance near the focal position, indicating typical reverse saturable absorption behavior. The decrease becomes more pronounced with increasing incident pulse energy, confirming enhanced nonlinear absorption at higher excitation intensity.

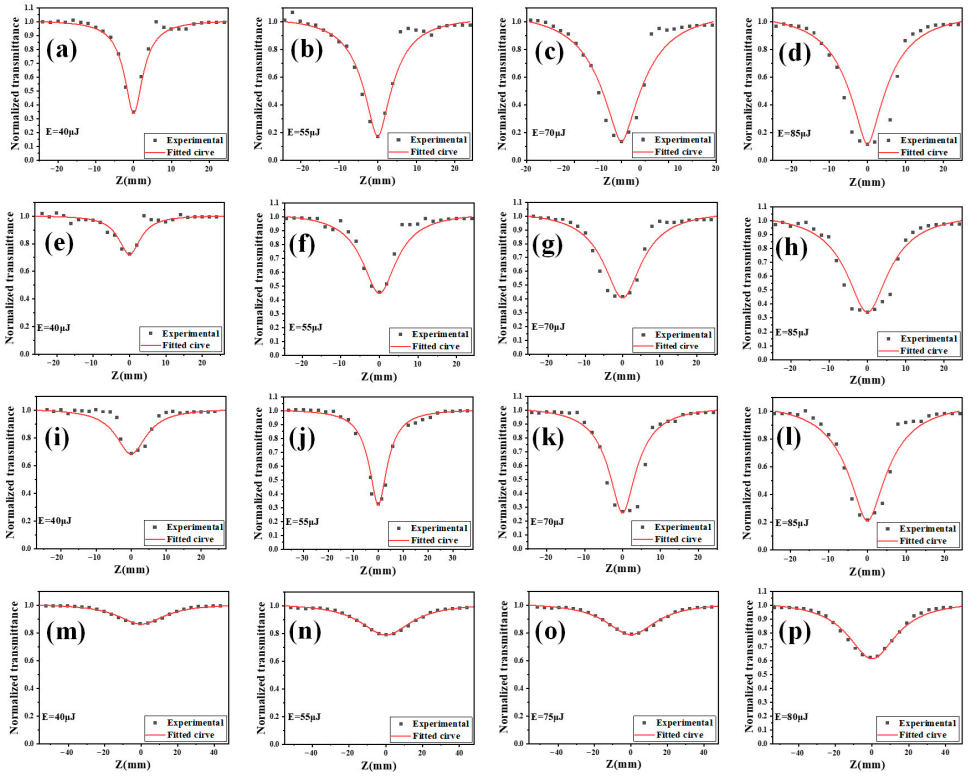


Figure 7. Open-aperture Z-scan curves of the MoS_2/PMMA organic-glass samples at incident pulse energies of 40 μJ, 55 μJ, 70 μJ, and 85 μJ: (**a**–**d**) MoS_2–MeCN6.5/PMMA, (**e**–**h**) MoS_2–MeCN4.5/PMMA, (**i**–**l**) MoS_2–$Na_2SO_4$6.5/PMMA, and (**m**–**p**) MoS_2–$Na_2SO_4$4.5/PMMA.

Among the samples, MoS_2–MeCN6.5/PMMA shows the strongest RSA response, whereas MoS_2–$Na_2SO_4$4.5/PMMA exhibits the weakest response. This trend is consistent with the structural and chemical characterization results. The better preserved MoS_2 lattice and lower oxidation level in the MeCN/TPABr-derived samples favor stronger nonlinear absorption, whereas oxidation and structural disorder in the aqueous-Na_2SO_4-derived samples reduce the effective active MoS_2 contribution.

The extracted β values are summarized in Figure 8. For all samples, β increases with incident pulse energy, indicating an intensity-dependent nonlinear absorption response. The MoS_2–MeCN6.5/PMMA sample exhibits the highest β value, reaching approximately 122 m GW^{-1} at 85 μJ. In contrast, the MoS_2–$Na_2SO_4$4.5/PMMA sample shows the lowest β value.

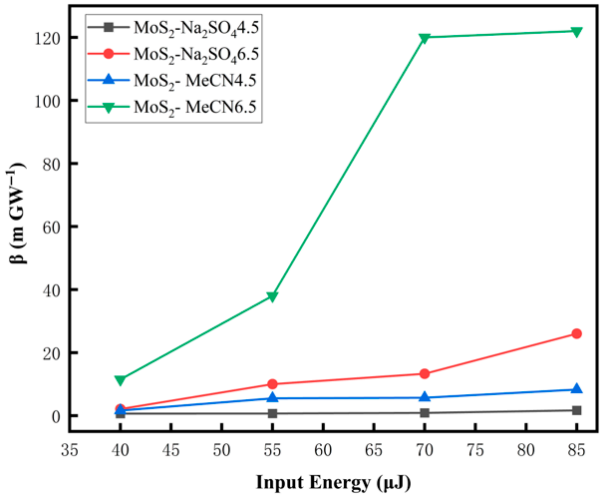


Figure 8. Nonlinear absorption coefficient (β) curves of the MoS_2/PMMA organic-glass samples at incident pulse energies of 40 μJ, 55 μJ, 70 μJ, and 85 μJ: MoS_2–MeCN6.5/PMMA, MoS_2–MeCN4.5/PMMA, MoS_2-$Na_2SO_4$6.5/PMMA, and MoS_2–$Na_2SO_4$4.5/PMMA.

The higher β value of the MeCN6.5 sample can be attributed to more effective exfoliation, better crystallinity, and suppressed oxidation, which collectively enhance excited-state absorption and carrier-related nonlinear absorption processes. These results indicate that increasing the applied voltage can improve the nonlinear optical response, but this effect is strongly dependent on the electrolyte environment.

3.4. Optical Limiting Performance and Structure–Property Correlation

The optical limiting performance of the MoS_2/PMMA composites was further evaluated, as shown in Figure 9; all samples exhibit a monotonic decrease in transmittance with increasing fluence, confirming their optical limiting capability [25].

The optical limiting threshold $F_{0.5}$ is defined as the incident fluence at which the normalized transmittance decreases to 50% of its initial value [26,27]. The MeCN/TPABr-derived samples generally show lower $F_{0.5}$ values than the aqueous-Na_2SO_4-derived samples, indicating better optical limiting performance [28].

Interestingly, the nonlinear absorption coefficient (β) and optical limiting threshold ($F_{0.5}$) are not strictly correlated. The MeCN6.5 sample shows the highest β but not the lowest $F_{0.5}$. This discrepancy arises because β reflects intrinsic third-order nonlinear absorption, whereas optical limiting behavior is influenced by additional factors such as scattering, thermal effects, and morphology-dependent light–matter interactions [29–31]

It should be noted that β and $F_{0.5}$ are not strictly proportional. While β mainly reflects the effective nonlinear absorption response extracted from Z-scan fitting, optical limiting performance is also influenced by scattering, thermal accumulation, morphology-dependent light propagation, and composite uniformity [29–31]. Therefore, the slightly different trends between β and $F_{0.5}$ are reasonable.

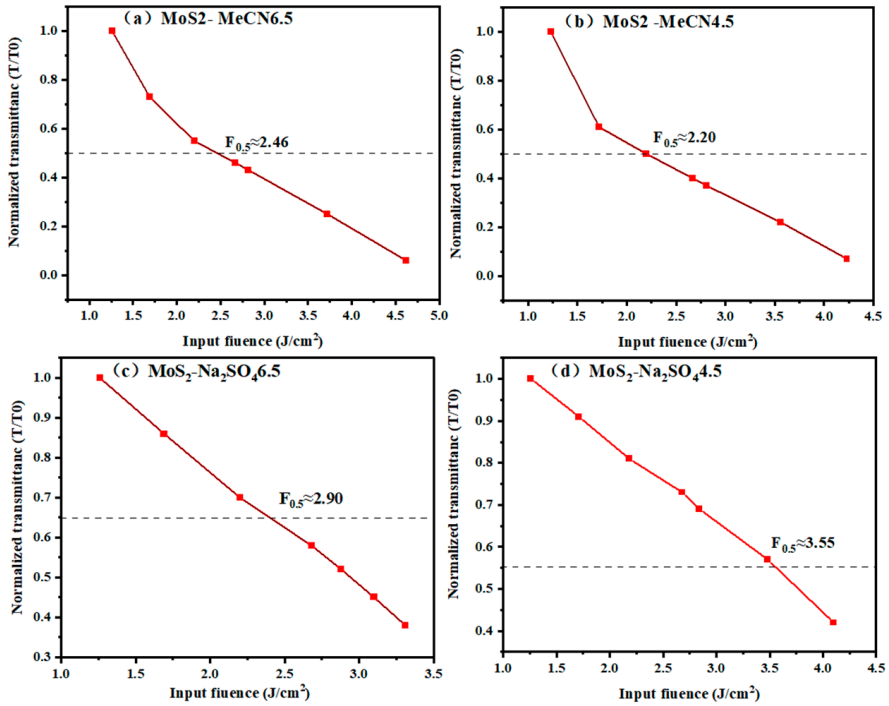


Figure 9. Optical limiting curves of MoS_2/PMMA organic glass samples prepared using different electrolyte systems and applied voltages: (**a**) MoS_2–MeCN6.5/PMMA; (**b**) MoS_2–MeCN4.5/PMMA; (**c**) MoS_2–$Na_2SO_4$6.5/PMMA; and (**d**) MoS_2–$Na_2SO_4$4.5/PMMA.

3.5. Mechanism–Structure–Property Relationship

Based on the above results, an electrolyte- and voltage-regulated mechanism–structure–property relationship can be proposed. In the nonaqueous MeCN/TPABr system, exfoliation is mainly associated with ion intercalation. A higher cathodic voltage facilitates ion insertion and interlayer decoupling, while the nonaqueous environment suppresses water-related oxidation. As a result, the obtained nanosheets retain better crystallinity and lower fractions of oxidized species, with Mo atoms predominantly remaining in the Mo^{4+} state.

In the aqueous Na_2SO_4 system, exfoliation is mainly related to bubble-assisted layer expansion. Increasing the applied voltage enhances gas evolution and improves exfoliation efficiency. However, the presence of water promotes oxidation-related side reactions, leading to the formation of multiple oxidation states, including Mo^{5+} and Mo^{6+}. The coexistence of these species suggests a progressive oxidation process from Mo^{4+} to higher valence states during electrochemical exfoliation.

Such oxidation-induced chemical-state evolution can introduce defect states, modify the local electronic structure, and reduce the effective MoS_2 active phase content. Consequently, the aqueous-Na_2SO_4-derived samples exhibit weaker nonlinear optical responses compared with the MeCN/TPABr-derived samples.

Therefore, the electrolyte determines the dominant exfoliation pathway, while the applied voltage regulates exfoliation efficiency and the extent of oxidation (including the relative fractions of Mo^{4+}, Mo^{5+}, and Mo^{6+}). These factors collectively govern the structural characteristics and nonlinear optical performance of the MoS_2/PMMA composites.

4. Conclusions

In this work, few-layer MoS_2 nanosheets were prepared by electrochemical exfoliation in nonaqueous MeCN/TPABr and aqueous Na_2SO_4 electrolyte systems under different applied voltages. The results show that the electrolyte environment determines the domi-

nant exfoliation pathway, while the applied voltage further regulates exfoliation efficiency, oxidation level, and structural preservation. The XPS results further reveal the coexistence of Mo^{4+}, Mo^{5+}, and Mo^{6+} species, indicating a progressive oxidation evolution during electrochemical exfoliation.

In the MeCN/TPABr system, exfoliation is mainly associated with ion intercalation, which promotes interlayer decoupling while suppressing oxidation. Consequently, the MeCN/TPABr-derived samples exhibit better crystallinity, lower oxidation, and stronger nonlinear absorption. In the aqueous Na_2SO_4 system, exfoliation is mainly driven by bubble-assisted expansion. Although higher voltage improves exfoliation efficiency, oxidation and structural disorder are still more pronounced than in the nonaqueous system.

Open-aperture Z-scan measurements show that all MoS_2/PMMA composites exhibit reverse saturable absorption and optical limiting behavior. The MoS_2–MeCN6.5/PMMA sample shows the strongest nonlinear absorption response, whereas the aqueous-Na_2SO_4-derived samples display relatively weaker performance due to increased oxidation and reduced effective MoS_2 active phase content. The difference between β and $F_{0.5}$ further indicates that intrinsic nonlinear absorption and device-level optical limiting are governed by related but distinct factors.

Overall, this study establishes a mechanism–structure–property relationship for electrochemically exfoliated MoS_2 nanosheets and demonstrates that electrolyte and voltage regulation are effective strategies for tuning MoS_2-based nonlinear optical materials.

Author Contributions: Conceptualization, X.F.; Methodology, X.C.; Software, B.L., J.P. and D.Z.; Validation, B.L., L.G., D.Z., S.L. and H.N.; Investigation, X.C. and S.Q.; Resources, L.G., H.N., X.F. and X.Y.; Data curation, S.Q., J.P., C.W. and F.P.; Writing—original draft, X.C.; Writing—review & editing, S.Q., H.Z., C.W., S.L., F.P., X.F. and X.Y.; Visualization, X.Y.; Supervision, H.Z.; Project administration, H.Z.; Funding acquisition, X.C. All authors have read and agreed to the published version of the manuscript.

Funding: This work was supported by Science and Technology Development Project of Jilin Province, China (No. 20240404047ZP).

Data Availability Statement: The original contributions presented in this study are included in the article. Further inquiries can be directed to the corresponding author(s).

Acknowledgments: During the preparation of this manuscript/study, the author(s) used ChatGPT 5.3 for the purposes of language polishing and grammar improvement. The authors have reviewed and edited the output and take full responsibility for the content of this publication.

Conflicts of Interest: The authors declare no conflict of interest.

References

1. Mak, K.F.; Lee, C.; Hone, J.; Shan, J.; Heinz, T.F. Atomically thin MoS_2: A new direct-gap semiconductor. *Phys. Rev. Lett.* **2010**, *105*, 136805. [CrossRef]
2. Wang, Q.H.; Kalantar-Zadeh, K.; Kis, A.; Coleman, J.N.; Strano, M.S. Electronics and optoelectronics of two-dimensional transition metal dichalcogenides. *Nat. Nanotechnol.* **2012**, *7*, 699–712. [CrossRef]
3. Splendiani, A.; Sun, L.; Zhang, Y.; Li, T.; Kim, J.; Chim, C.-Y.; Galli, G.; Wang, F. Emerging photoluminescence in monolayer MoS_2. *Nano Lett.* **2010**, *10*, 1271–1275. [CrossRef]
4. Zheng, W.; Lee, L.Y.S. Beyond sonication: Advanced exfoliation methods for scalable production of 2D materials. *Matter* **2022**, *5*, 515–545. [CrossRef]
5. Duan, X.; Zhang, H. Introduction: Two-dimensional layered transition metal dichalcogenides. *Chem. Rev.* **2024**, *124*, 10619–10622. [CrossRef]
6. Nicolosi, V.; Chhowalla, M.; Kanatzidis, M.G.; Strano, M.S.; Coleman, J.N. Liquid exfoliation of layered materials. *Science* **2013**, *340*, 1226419. [CrossRef]

7. Saliba, M.; Atanas, J.P.; Howayek, T.M.; Habchi, R. Molybdenum disulfide, exfoliation methods and applications to photocatalysis: A review. *Nanoscale Adv.* **2023**, *5*, 6787–6803. [CrossRef]
8. Zhao, M.; Casiraghi, C.; Parvez, K. Electrochemical exfoliation of 2D materials beyond graphene. *Chem. Soc. Rev.* **2024**, *53*, 3036–3064. [CrossRef] [PubMed]
9. Wang, Y.; Zhang, K.; Zhao, Y.; Wu, Z.-H.; Zhou, Y.-Y.; Li, S.-L.; Wu, X.-Q.; Li, L.; Ke, C.; Xu, L.; et al. Comprehensive review of novel two-dimensional fullerene network: Synthesis, theoretical investigations, and applications. *Rare Met.* **2025**, *44*, 9726–9746. [CrossRef]
10. Tang, B.; Sivan, M.; Leong, J.F.; Xu, Z.; Zhang, Y.; Li, J.; Wan, R.; Wan, Q.; Zamburg, E.; Thean, A.V.-Y. Solution-processable 2D materials for monolithic 3D memory-sensing-computing platforms: Opportunities and challenges. *npj 2D Mater. Appl.* **2024**, *8*, 74. [CrossRef]
11. Lin, Z.; Wan, Z.; Song, F.; Huang, B.; Jia, C.; Qian, Q.; Kang, J.S.; Wu, Y.; Yan, X.; Peng, L.; et al. High-yield exfoliation of 2D semiconductor monolayers and reassembly of organic/inorganic artificial superlattices. *Chem* **2021**, *7*, 1887–1902. [CrossRef]
12. Wang, S.; Xue, J.; Xu, D.; He, J.; Dai, Y.; Xia, T.; Huang, Y.; He, Q.; Duan, X.; Lin, Z. Electrochemical molecular intercalation and exfoliation of solution-processable two-dimensional crystals. *Nat. Protoc.* **2023**, *18*, 2814–2837. [CrossRef]
13. Coşkun, A.; Kopar, A.S.; Özerbaş, Z.E.; Işık, M.A.; Erişmiş, K.Ö.; An, M.; Çağlar, M.A.; Çakmak, B.; Ertuğrul, M.; Turgut, G. Experimental insights into characteristic properties and applications of two-dimensional Janus transition metal dichalcogenide materials: A comprehensive review. *Rare Met.* **2025**, *44*, 8161–8197. [CrossRef]
14. Tao, L.; Long, H.; Zhou, B.; Yu, S.F.; Lau, S.P.; Chai, Y.; Fung, K.H.; Tsang, Y.H.; Yao, J.; Xu, D. Preparation and characterization of few-layer MoS_2 nanosheets and their good nonlinear optical responses in the PMMA matrix. *Nanoscale* **2014**, *6*, 9713–9719. [CrossRef] [PubMed]
15. Liu, Q.; Liu, J.-G.; Liu, J.-Y.; Zhou, B.-J.; Liu, Q.-Y.; Liu, Y.; Zhao, Y.-Q.; Jiang, S.-L. Raman scattering of two-dimensional MoO_2 flakes at high pressure. *Rare Met.* **2025**, *44*, 2830–2835. [CrossRef]
16. Dhasmana, N.; Fadil, D.; Kaul, A.B.; Thomas, J. Investigation of nonlinear optical properties of exfoliated MoS_2 using photoacoustic Z-scan. *MRS Adv.* **2016**, *1*, 3215–3221. [CrossRef]
17. He, M.; Quan, C.; He, C.; Huang, Y.; Zhu, L.; Yao, Z.; Zhang, S.; Bai, J.; Xu, X. Enhanced nonlinear saturable absorption of MoS_2/graphene nanocomposite films. *J. Phys. Chem. C* **2017**, *121*, 27147–27153. [CrossRef]
18. Zhang, S.; Dong, N.; McEvoy, N.; O'Brien, M.; Winters, S.; Berner, N.C.; Yim, C.; Li, Y.; Zhang, X.; Chen, Z.; et al. Direct observation of degenerate two-photon absorption and its saturation in WS_2 and MoS_2 monolayer and few-layer films. *ACS Nano* **2015**, *9*, 7142–7150. [CrossRef]
19. Rafi, R.; Rahulan, K.M.; Flower, N.A.L.; Abith, M.; Chidambaram, S.G.T.; Rajendran, A.S. Optical limiting performance of MoS_2 nanosheets exfoliated via liquid-phase sonication: Implications for laser shielding. *ACS Appl. Nano Mater.* **2024**, *7*, 11097–11106. [CrossRef]
20. Wang, H.-S.; Su, S.-P.; Huang, Y.-H.; Tu, L.-W.; Wadekar, P.V.; Wang, H.-C.; Lee, C.-K. Investigation of 2H/1T/1T′ phase MoS_2 optical nonlinearity. *Discov. Nano* **2025**, *20*, 129. [CrossRef]
21. Ajami, A.; Ovsianikov, A.; Liska, R.; Baudis, S. Z-scan technique: A review from conventional Z-scan to white light Z-scan. *Appl. Phys. B* **2024**, *130*, 138. [CrossRef]
22. Volpi, A.; Kock, J.; Albrecht, A.R.; Hehlen, M.P.; Epstein, R.I.; Sheik-Bahae, M. Open-aperture Z-scan study for absorption saturation: Accurate measurement of saturation intensity in YLF:Yb for optical refrigeration. *Opt. Lett.* **2021**, *46*, 1421–1424. [CrossRef]
23. Liu, Y.; Wang, F.; Li, L.; Cao, F.; Zhu, B.; Gu, Y. Linear and nonlinear optical properties of AgNPs and AgNPs/graphene composites modulated by localized surface plasmon resonance effect. *J. Opt. Soc. Am. B* **2022**, *39*, 713–721. [CrossRef]
24. Yan, H.; Li, B.; Pan, J.; Fang, X.; Yu, Y.; Wang, D.; Fang, D.; Zhan, Y.; Wang, X.; Li, J.; et al. Controlling the crystallinity and morphology of bismuth selenide via electrochemical exfoliation for tailored reverse saturable absorption and optical limiting. *Nanomaterials* **2025**, *15*, 52. [CrossRef]
25. Stavrou, M.; Chazapis, N.; Nikoli, E.; Arenal, R.; Tagmatarchis, N.; Couris, S. Crystalline phase effects on the nonlinear optical response of MoS_2 and WS_2 nanosheets: Implications for photonic and optoelectronic applications. *ACS Appl. Nano Mater.* **2022**, *5*, 16674–16686. [CrossRef]
26. Sirohi, S.; Jaiswal, M.; Bisht, P.B. Mixed phase MoS2 quantum dots as optical limiters for ultrafast lasers. *ACS Appl. Nano Mater.* **2024**, *7*, 7142–7153. [CrossRef]
27. Shang, L.; Wu, S.; Liu, X.; Duan, Y.; Li, Y.; Duan, Q. Novel structure and excellent nonlinear optical performance nanocomposite derived from flower-like MOF grown on MoS_2. *Dyes Pigments* **2024**, *225*, 112089. [CrossRef]
28. Dandasena, B.; Das, S.; Kumar, P.C.; Supriya, S.; Naik, R. VS_2/MoS_2 nanocomposite with reverse saturable absorption for optical limiting and nonlinear optical applications. *J. Appl. Phys.* **2025**, *137*, 043101. [CrossRef]
29. Du, B.; Zhao, Z.; Xin, Y.; Ren, Z.; Xing, F.; Zhang, F. 2D Ti_3AlC_2 and Ti_3C_2 nanosheets: Excellent optical limiting materials for laser protection. *Opt. Mater.* **2024**, *147*, 114691. [CrossRef]

30. Chen, B.; Fang, D.; Chen, L.; Shen, X.; Wei, J.; Wang, D.; Zhang, Q.; Ouyang, Q.; Fang, X.; Chen, X. Adjusting the nonlinear optical and optical limiting properties of $MAPbBr_3$/PMMA by doping with Zn. *Mater. Chem. Phys.* **2023**, *309*, 128310. [CrossRef]
31. Ding, C.; Shao, C.; Wang, Z.; Li, Z.; Guo, X.; Ren, X.; Pei, H.; Wu, S.; Zhang, Q.; Wei, C.; et al. Leaf vein micronetwork engineering enhanced energy conversion strategy for C-band ultralight yet tunable microwave absorption. *Rare Met.* **2025**, *44*, 6513–6530. [CrossRef]

Disclaimer/Publisher's Note: The statements, opinions and data contained in all publications are solely those of the individual author(s) and contributor(s) and not of MDPI and/or the editor(s). MDPI and/or the editor(s) disclaim responsibility for any injury to people or property resulting from any ideas, methods, instructions or products referred to in the content.